Research Square

# Sharp kinetic acceleration potentials during mediated redox catalysis of insulators

**Deqing Cao**
  Nanjing Tech University

**Xiaoxiao Shen**
  Nanjing Tech University

**Aiping Wang**
  Shanghai University

**Fengjiao Yu**
  Nanjing Tech University

**Yuping Wu**
  Nanjing Tech University

**Siqi Shi**
  Shanghai University

**Stefan Freunberger** ( ✉ stefan.freunberger@ist.ac.at )
  Institute of Science and Technology Austria    https://orcid.org/0000-0003-2902-5319

**Yuhui Chen**
  Nanjing Tech University

**Article**

**Keywords:**

# Sharp kinetic acceleration potentials during mediated redox catalysis of insulators

Deqing Cao[1][+], Xiaoxiao Shen[1][+], Aiping Wang[2], Fengjiao Yu[1], Yuping Wu[1], Siqi Shi[2,4]*, Stefan A. Freunberger[3]*, Yuhui Chen[1]*

[1] State Key Laboratory of Materials-oriented Chemical Engineering, College of Chemical Engineering, Nanjing Tech University, Nanjing, Jiangsu, 211816 China

[2] School of Materials Science and Engineering, Shanghai University, Shanghai 200444, China

[3] IST Austria (Institute of Science and Technology Austria), Klosterneuburg, Austria

[4] Materials Genome Institute, Shanghai University, Shanghai 200444, China

Corresponding authors: cheny@njtech.edu.cn; sqshi@shu.edu.cn; stefan.freunberger@ist.ac.at

[+] Authors contributed equally to this work.

**Redox mediators could catalyse otherwise slow and energy-inefficient cycling of Li-S and Li-O$_2$ batteries by shuttling electrons/holes between the electrode and the solid insulating storage materials. For mediators to work efficiently they need to oxidize the solid with fast kinetics yet the lowest possible overpotential. Here, we found that when the redox potentials of mediators are tuned via, e.g., Li$^+$ concentration in the electrolyte, they exhibit distinct threshold potentials, where the kinetics accelerate several-fold within a range as small as 10 mV. This phenomenon is independent of types of mediators and electrolyte. The acceleration originates from the overpotentials required to activate fast Li$^+$/e$^-$ extraction and the following chemical step at specific abundant surface facets. Efficient redox catalysis at insulating solids requires therefore carefully considering the surface conditions of the storage materials and electrolyte-dependent redox potentials, which may be tuned by salt concentrations or solvents.**

26    Electrochemistry with insulators is salient feature and central difficulty of topical future

27    battery chemistries such as Li-air (O$_2$), Li-CO$_2$, Li-Sulphur (Li-S) cells[1-10]. They differ in this respect

28    from current intercalation-type batteries, which rely on ion (de)insertion to balance charge upon

29    redox of the mixed-conducting solid host[1]. The interest in Li-O$_2$, -CO$_2$, and -S cells arises from high

30    theoretical energies, abundant elements, low cost and environmental friendliness. Li-O$_2$/CO$_2$ cells

31    interconvert O$_2$ dissolved in the electrolyte into solid, insulating Li$_2$O$_2$ or Li$_2$CO$_3$ during

32    discharge/charge. Li-S batteries interconvert solid, insulating S$_8$ and Li$_2$S. Kinetic bottleneck during

33    these processes is charge transfer between electrode and the insulating, insoluble, solid storage

34    materials, causing high overpotentials and incomplete conversion even at low rates.

35    Redox catalysis using mediators can bypass those insulators, transporting charge through the

36    electrolyte phase where ion and electron/hole transport may be facile and may boost charge

37    transfer kinetics[3-5,11-14]. Equally important is to approach the cycling potential as close as possible

38    towards the formal potential of the storage material to maximize energy efficiency and to suppress

39    parasitic reactions[4,5,15-21]. Soluble redox mediators (RMs) are, therefore, now accepted to be key to

40    achieve these goals and have been studied in a wide variety for Li-O$_2$ cells[3-5,11-13,18,21-24]. First

41    examples have been reported for S electrochemistry[3,25-27]. Redox mediation on, for example,

42    charging involves oxidizing the mediator RM$^{red}$ at the electrode surface to its oxidized form RM$^{ox}$,

43    its diffusion to the surface of Li$_2$O$_2$ or Li$_2$S, where RM$^{ox}$ extracts charge and reforms RM$^{red}$. Main

44    requirements for successful redox catalysis include a suitable equilibrium potential of the redox

45    couple to drive the reaction and fast heterogeneous reaction rates between RM and both electrode

46    ($k^0$) and storage material. $k^0$ is sufficiently fast[28] and well described by established theories of

47    electron transfer between redox molecule and metallic conductor[29]. However, for the rate limiting

48    electron transfer between RM$^{ox}$ and a redox active insulating solid, despite being essential, detailed

49    descriptors are missing.

50    Activating this most difficult electron transfer step is the primary goal of redox catalysis on

51    charging Li-S and Li-O$_2$ batteries, which have important parallels in their charging reactions. The

52    insulating Li$_2$S and Li$_2$O$_2$ undergo in a first step a one-electron oxidation to form Li polysulfides

53    (LiPSs) or Li superoxide (LiO$_2$) intermediates. Further oxidation and/or disproportionation

54    eventually yields the most oxidized forms S$_8$ and O$_2$, respectively[10,20,30-32]. Reaction kinetics for RM$^{ox}$

55    and Li$_2$O$_2$ were reported for a range of mediators, typically assuming faster kinetics with higher

56    mediator potential (driving force)[28,33,34]. Impacts of solvents have been noted on the redox

57    potentials of mediators and the Li/Li$^+$ redox couple[15,35]. For mediated Li$_2$S oxidation, faster

58    mediated compared to unmediated kinetics were phenomenologically inferred from potentiostatic

59    titration or galvanostatic cycling[25-27]. However, quantitative relations between electrolyte-

60    dependent redox potentials of mediators and the kinetics of mediated oxidation of insulating solids

61    are missing, yet this knowledge is essential for mediated redox catalysis of insulators.

62    Here, we investigate the kinetics of mediated Li$_2$S and Li$_2$O$_2$ oxidation upon varying the redox

63    potential of particular mediators by means of Li$^+$ concentration and electrolyte solvent. We find

64    that the kinetics show distinct threshold potentials, where the kinetics accelerates several-fold

65    within a voltage range of as little as 10 mV. We show that the thresholds originate from the

66  overpotentials to activate fast Li$^+$/e$^-$ extraction followed chemical steps. Overpotentials are
67  different amongst facets and, therefore, thresholds indicate abundant facets.

68  **Results**

69  **Thresholds in the potential-dependent kinetics of RMs oxidizing Li$_2$S and Li$_2$O$_2$**

70  Decamethyl ferrocene (DFc) and lithium iodide (LiI) are commonly used RMs for the charging
71  process in Li-S batteries and Li-O$_2$ batteries, respectively, and thus they are chosen as model RMs
72  in this work[14]. Their redox potentials, $E_{\text{DFc/DFc}^+}$ and $E_{\text{I}^-/\text{I}_3^-}$, measured on the AgCl/Ag scale are
73  nearly independent of Li$^+$ concentration because of the species' large radii and weak solvation,
74  while $E_{\text{Li/Li}^+}$ does vary with Li$^+$ concentration following Nernst equation. Hence, $E_{\text{DFc/DFc}^+}$ and
75  $E_{\text{I}^-/\text{I}_3^-}$ vs Li/Li$^+$ vary with Li$^+$ concentration as shown in Supplementary Fig. 1.

76  Figure 1 shows the potential-dependent apparent rate constants $k^{\text{app}}$ of DFc$^+$ and I$_3^-$
77  oxidizing Li$_2$S and Li$_2$O$_2$, respectively. The rate constant for DFc$^+$ oxidizing Li$_2$S ($k^{\text{app}}_{\text{DFc}-\text{Li}_2\text{S}}$) was
78  measured by following the DFc$^+$ concentration of a solution in contact with Li$_2$S using UV-Vis
79  spectroscopy (see Methods and Supplementary Figure S2). The rate constant of I$_3^-$ oxidizing Li$_2$O$_2$
80  ($k^{\text{app}}_{\text{I}_3^--\text{Li}_2\text{O}_2}$) was measured using both scanning electrochemical microscopy (SECM) and differential
81  electrochemical mass spectrometry (DEMS) as detailed in Supplementary Note 1. Given the
82  complex mechanism with initial oxidation of Li$_2$S or Li$_2$O followed by further oxidation of the
83  intermediates or their disproportionation, apparent rate constants embrace all e$^-$ transfer steps. In
84  either case, the rates followed first-order behaviour in RM$^{\text{ox}}$ concentration. They increase with
85  increasing mediator equilibrium potential. Surprisingly, however, is that in both cases kinetics
86  increased sharply by a factor of ~3 to 4.4 over a certain narrow range of equilibrium potentials,
87  whereas changes were gradual below and above these potentials. They represents a threshold,
88  where rather slow kinetics at lower potentials switches to much higher levels.
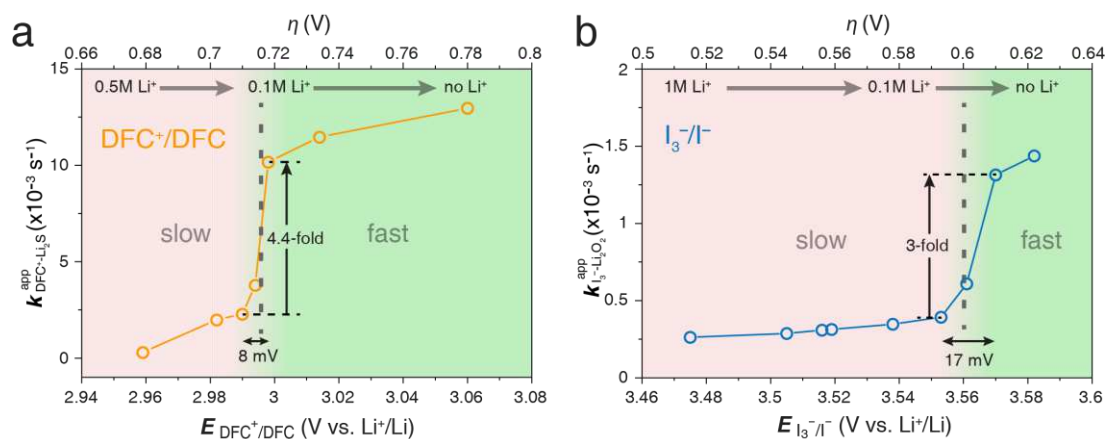


90  **Fig. 1 | Potential-dependent kinetics of mediated oxidation of Li$_2$S and Li$_2$O$_2$. a, b**, The apparent reaction rate
91  constants ($k^{\text{app}}$) of as a function of the equilibrium potentials of the mediators. **a**, $k^{\text{app}}_{\text{DFc}-\text{Li}_2\text{S}}$ of decamethyl
92  ferrocene (DFc$^+$) oxidizing Li$_2$S with the equilibrium potentials ($E_{\text{DFc/DFc}^+}$) tuned by the Li$^+$ concentration as
93  indicated. The electrolyte was DME containing LiTFSI. The ordinate on the top indicates the overpotential relative
94  to Li$_2$S/Li$_2$S$_2$. **b**, Equivalent data for I$_3^-$ oxidizing Li$_2$O$_2$ ($k^{\text{app}}_{\text{I}_3^--\text{Li}_2\text{O}_2}$) with various $E_{\text{I}^-/\text{I}_3^-}$ in DMSO electrolyte containing
95  LiTFSI. Thresholds were identified at 2.995 V and 3.56 V vs. Li$^+$/Li, respectively.

96    For DFc⁺ oxidizing Li₂S, this distinct threshold was at ~2.995 V vs. Li/Li⁺ in 1,2-dimethoxyethane
97    (DME), Fig. 1a. When the Li⁺ concentration decreased from 0.15 M to 0.1 M, $E_{\text{DFc/DFc}^+}$ only
98    slightly increased by 8 mV to 2.998 V, while $k_{\text{DFc}-\text{Li}_2\text{S}}^{\text{app}}$ was boosted 4.4-fold from 0.0023 to
99    0.0102 s⁻¹. This threshold corresponds to an overpotential of ~0.72 V versus the equilibrium
100   potential of the Li₂S/Li₂S₂ redox couple, the relevant reaction for the first electron transfer step. As
101   a multi-step reaction, the reaction mechanism of Li₂S oxidation is complicated and forms as a first
102   step partly soluble Li₂S₂ species as intermediate, which then over a series of
103   oxidation/disproportionation steps eventually forms S₈. Therefore, the apparent kinetics could be
104   dominated by the oxidation of either solid Li₂S or soluble polysulfides. To identify the rate-
105   determining step, DFc⁺ solutions in DME were separately added to two cuvettes with solid Li₂S and
106   Li polysulfide dissolved in DME. The UV-vis spectra of both solutions were recorded after reacting
107   for 150 s. As shown in Supplementary Fig. 3, DFc⁺ was completely consumed in the reaction with
108   polysulphides, but only partly with Li₂S, which indicates that the reaction of DFc⁺ oxidizing solid
109   Li₂S is slower than oxidizing polysulfides and thus the former is the rate-determining step.
110   Therefore, the threshold of $E_{\text{DFc/DFc}^+}$ at 2.995 V in Fig. 1a is associated with the reaction of DFc⁺
111   oxidizing solid Li₂S instead of oxidizing soluble polysulfides.

112   Turning to I₃⁻ oxidizing Li₂O₂, a similar threshold was found around 3.56 V vs. Li⁺/Li (between
113   0.05 and 0.01 M Li⁺), where the kinetics is accelerated 3-fold over only 17 mV. Our previous work
114   has shown that, again, the first electron extraction to form a superoxide is the rate determining
115   step[20] and, therefore, the threshold of ~3.56 V in Fig. 1b is associated with I₃⁻ oxidizing solid Li₂O₂.

116   **Factors governing the thresholds**

117   These astonishing but unambiguous thresholds of $E_{\text{RM}^{\text{red}}/\text{RM}^{\text{ox}}}$ at 2.995 V for Li₂S and 3.56
118   V for Li₂O₂ could originate from many factors such as electrolytes, type of RM, or surface properties
119   of Li₂S and Li₂O₂. We focus further on Li₂O₂ oxidation. Given that Li⁺ is not involved in the I₃⁻/I⁻
120   redox couple, $E_{\text{I}^-/\text{I}_3^-}$ relies on the Li⁺ activity ($a_{\text{Li}^+}$) in the electrolyte as detailed in Supplementary
121   Note 2. It can be manipulated either by directly changing the Li⁺ concentration in a given solvent
122   or by changing the solvation ability of the electrolyte[35], which changes the activity coefficient ($\gamma$)
123   and $a_{\text{Li}^+}$. To prove this, a dimethyl sulfoxide (DMSO)/DME mixture electrolyte with various ratios
124   of DMSO/DME and constant 10 mM Li⁺ was used to change the solvation of Li⁺ and thus to
125   manipulate $E_{\text{I}^-/\text{I}_3^-}$ (Supplementary Fig. 4). Figure 2a compares the resulting apparent kinetics
126   versus $E_{\text{I}^-/\text{I}_3^-}$ with those obtained with varying Li⁺ concentrations in pure DMSO. Although tuned
127   differently, an analogous step-change in kinetics at 3.56 V resulted. For example, 10 mM Li⁺ in
128   DMSO yielded a potential beyond the threshold and fast kinetics while increasing DME raised Li⁺
129   activity and lowered the potential below the threshold. As the extreme, I₃⁻ in contact with Li₂O₂ in
130   pure DME evolved almost no O₂, Supplementary Fig. 5. Changing kinetics is, hence, not simply
131   arising from the solvent or Li⁺ concentration, but rather from $a_{\text{Li}^+}$ and in turn the potential on
132   the Li/Li⁺ scale. We conclude that the thresholds is genuinely linked to $E_{\text{I}^-/\text{I}_3^-}$.
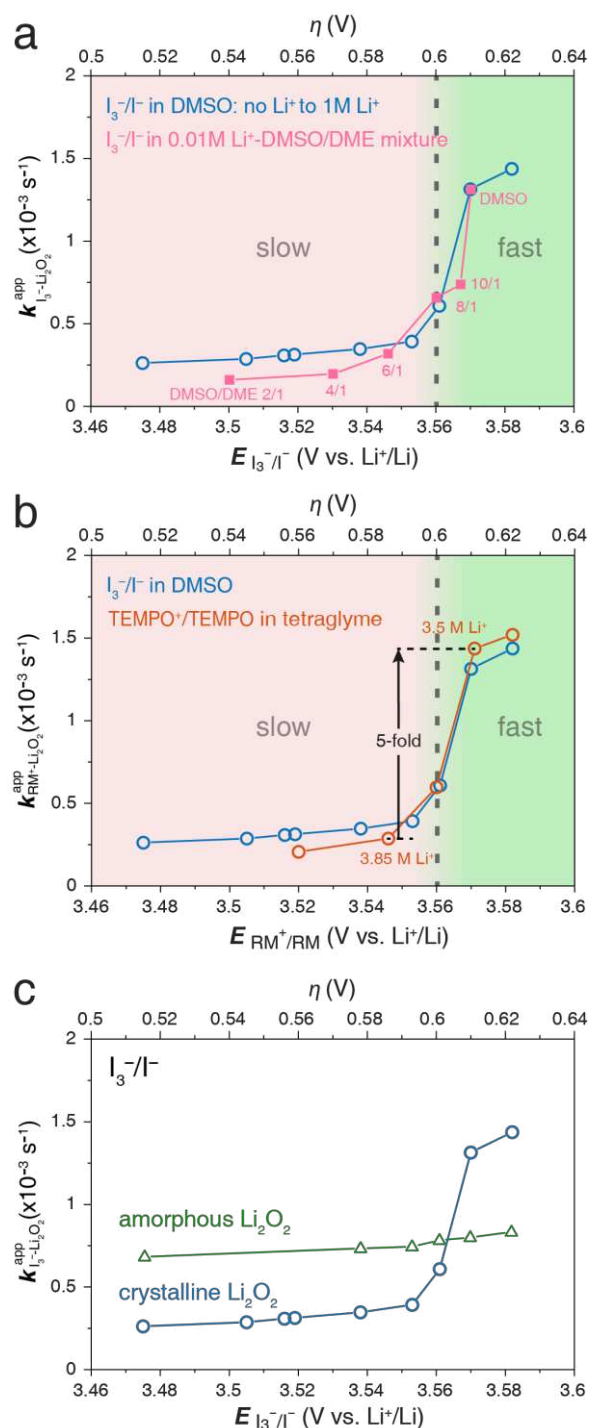
**Figure 2 | Potential-dependent kinetics of Li₂O₂ oxidation in various systems. a,** $I_3^-/I^-$ in DMSO and DMSO/DME mixtures with various ratios; **b,** TEMPO⁺/TEMPO in tetraglyme electrolytes with various Li⁺ concentrations. The dashed lines indicate the threshold potentials. **c,** rate constants $k_{I_3^--Li_2O_2}^{app}$ for oxidizing crystalline Li₂O₂ (blue) and amorphous Li₂O₂ (green) in DMSO solution with various Li⁺ concentrations.

To further prove the threshold to be linked to redox potential rather than the particular RM, the same experiments were carried out with 2,2,6,6-tetramethyl-1-piperidinyloxy (TEMPO) and tetraethylene glycol dimethyl ether (tetraglyme) to substitute for LiI and DMSO. Both TEMPO and tetraglyme have been extensively employed in the Li-O₂ batteries[18,19]. O₂ evolving from TEMPO⁺ in

143  contact with $Li_2O_2$ is shown in Supplementary Fig. 6 and the apparent kinetics in Fig. 2b, again
144  compared to the $I_3^-$/DMSO data. From 3.25 M to 4 M $Li^+$, $E_{\text{TEMPO/TEMPO}^+}$ varied from 3.58 V to 3.52
145  V, covering the previously determined threshold. Again, a similar step-change increasing kinetics
146  5-fold appeared at ~3.56 V. This result verifies the threshold to be independent of the type of RM
147  or solvent. We show in Supplementary Note 3 that thresholds do not stem from impurities.
148  Together with a similar threshold for $Li_2S$ oxidation at a different overpotential, we conclude that
149  the thresholds are linked to the intrinsic surface properties of solid $Li_2O_2$ or $Li_2S$ such as crystal
150  facets.

**The impact of facets**

152  We hypothesize that the exposed facets of solid $Li_2O_2$ determine the charge transfer kinetics
153  given the reaction takes place at the surface where certain crystal facets are preferentially exposed.
154  To confirm the impact of facets, we measured the potential-dependent kinetics of $I_3^-$ oxidizing
155  amorphous $Li_2O_2$ that lacks dominant facets and therefore should likely not show thresholds.
156  Amorphous $Li_2O_2$ was synthesized as described earlier and its amorphous state confirmed by XRD,
157  Supplementary Fig. 7[36]. Apparent kinetics $k_{I_3^- - Li_2O_2}^{\text{app}}$ is compared with the data from crystalline
158  $Li_2O_2$ in Fig. 2c and shows no sudden acceleration at 3.56 V, confirming the threshold at 3.56 V to
159  be associated with specific abundant facets of crystalline $Li_2O_2$.

160  To identify the exposed facets, the crystalline $Li_2O_2$ was examined with selected area electron
161  diffraction (SAED) in the transmission electron microscope (TEM). The SAED pattern taken down
162  the $[11\bar{2}0]$ zone axis, Supplementary Fig. 8b, is well indexed to $Li_2O_2$ (P63/mmc). The elongated
163  particle extends in [0001] direction with the $(11\bar{2}0)$ facet dominating the surface followed (0001),
164  Supplementary Fig. 8a. Given that these facets dominate the surface of the $Li_2O_2$ crystallites, their
165  properties should predominantly govern the kinetics.

**Thresholds for $(11\bar{2}0)$ and (0001) facets**

167  We further explored the chemistry underpinning the threshold potential for $Li_2O_2$ oxidation
168  using density functional theory (DFT) calculations. Particularly, we determined the overpotentials
169  needed to oxidize the dominating facets, in turn rationalizing the threshold potential to activate
170  fast oxidation pathways. We go beyond previous DFT work modelling $Li_2O_2$ oxidation, which only
171  allowed for full removals of the stoichiometric formula via electrochemical steps[37-40]. I.e., two $Li^+$
172  and one $O_2$ via either $-Li^+$, $-O_2$, $-Li^+$ or $-Li^+$, $-Li^+$, $-O_2$. However, recent experimental work
173  highlighted the dominance of superoxide disproportionation as the $O_2$ evolving step in general and
174  for the formation of the highly reactive singlet oxygen ($^1O_2$) in particular[17,20,31,41,42]. We therefore
175  explicitly allow for disproportionation as well. To do so, we did not limit the charging process to a
176  stoichiometric formula (i.e. two $Li^+$ per $O_2$), but allow for more than two $Li^+$ ions to be removed
177  before $O_2$ evolves.

178  Using the computational procedure detailed in the Methods, we calculated the reaction
179  energy for each intermediate reaction step. Steps are either electrochemical to desorb Li (one
180  electron and one $Li^+$) or chemical to desorb $O_2$. After each Li removal, the system relaxed to

181 equilibrium with the remaining atoms reorganizing, releasing the reorganization energy $\Delta E_{\text{reorg}}^{j}$

182 in the $j^{\text{th}}$ step and the entire slab assuming a new total energy $\Delta E^{j}$. Li is removed from the $Li_2O_2$

183 surface one after another with the assistance of an overpotential $\eta$. The energy $\Delta E_c^{j}$ required to

184 desorb $O_2$ chemically after removing $j$ Li indicates the ease of the overall process to desorb $j$ Li and

185 one $O_2$. At least two Li need to desorb before any O–O moiety could become superoxide-like. Hence,

186 $O_2$ desorbing after two Li would refer to direct oxidation of a peroxide moiety to $O_2$. $O_2$ desorbing

187 after removing four or more Li would refer to disproportionation, leaving behind a Li-deficient $Li_{2-}$

188 $_xO_2$ surface.

189     We examined the dominant $(11\overline{2}0)$ and $(0001)$ facets whose structures are shown in Fig. 3a,d.

190 The structural unit with the O–O dimer surrounded by six Li atoms is shown in Supplementary Fig.

191 9. Figures 3b,e give the relaxed energy $\Delta E^{j}$ after the $j^{\text{th}}$ Li removal for four overpotentials up to

192 the minimum overpotential required for up to seven Li removals to become smaller or equal to

193 zero. This number resulted from the number required for the relaxed bond length of one O–O

194 moiety to approach 1.23 Å as found in molecular $O_2$, Fig. 3c. This number also coincides with $\Delta E_c^{j}$

195 becoming lower than 0.2 eV, which is easily overcome thermally, Fig. 3f.
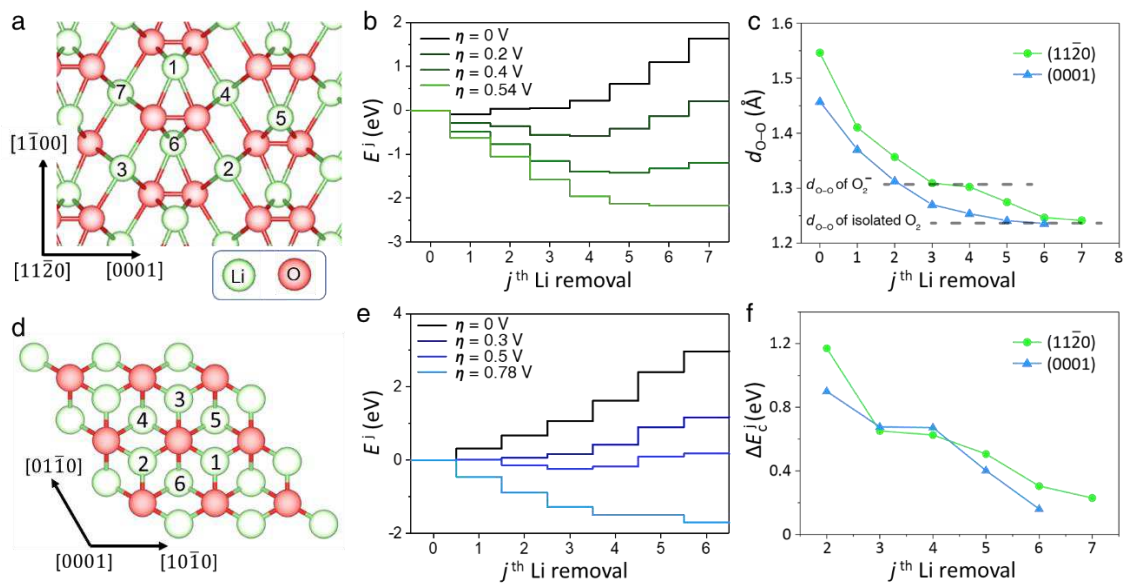


**Fig. 3 | The surface structures and energy profiles during oxidation of specific $Li_2O_2$ facets. a,b,** The surface
structure of the $(11\overline{2}0)$ facet including the succession of the lowest energy Li extractions (**a**) and the energy profiles
during these Li removals under various overpotentials ($\eta$). **d,e,** Equivalent surface structure and energy profiles for
the $(0001)$ facet. **c,** The evolution of O–O bond lengths of the central O–O moiety in these facets upon Li removal.
**f,** The evolution of the chemical energy required to desorb molecular $O_2$ after at least two Li extractions.

202     We consider first the $(11\overline{2}0)$ facet. With losing three Li, the O–O bond length gradually

203 shortened from 1.54 Å to 1.3 Å (indicating superoxide), Fig. 3c. After four Li removed, formally two

204 adjacent superoxides exist at the surface as also seen in the Bader charge, Supplementary Fig. 10b.

205 Since the $O_2$ desorption energy is with 0.6 eV still significant, spontaneous $O_2$ desorption appears

206 unlikely. However, after removing six to seven Li, the relaxed O–O bond length is close to the 1.23 Å

207 of molecular $O_2$, Fig. 3c, which is no longer strongly chemically bonded, Fig. 3f. Importantly, this

208 process can be interpreted as disproportionation. As indicated by the Bader charge after removing
209 beyond four Li, one of the two superoxide-like O–O moieties attracts the electron from the nearby
210 one and redistributes the remaining electrons on the surface between the neighbouring O–O
211 moieties. The redistribution is equally seen in the O–O bond lengths; while it decreases continually
212 for the central moiety, the neighbouring ones remain close to the lengths of initial peroxide,
213 Supplementary Fig. 10. This surface disproportionation leaves behind a Li-deficient $Li_2O_2$ surface
214 and an easily released $O_2$ molecule.

215 Figure 3b shows the corresponding reaction energy profiles for the electrochemical steps at
216 various overpotentials. A minimum overpotential of 0.54 V is required to make the process all the
217 way to seven Li removals energy-downhill, where $O_2$ is released most easily. Lower overpotentials
218 mean higher energy barriers for $O_2$ release, which is associated with low rates. Consequently, the
219 0.54 V are the overpotential required to activate an overall fast oxidation/$O_2$ release pathway at
220 the $(11\bar{2}0)$ facet. Given this facet to dominate, this overpotential accelerates the decomposition
221 of $Li_2O_2$. This calculation result agrees well with the threshold overpotential of 0.60 V identified in
222 experiments.

223 Turning to the (0001) facet, Fig. 3c, the O–O moiety is surrounded by six Li atoms. The energy
224 profiles, the O–O bond length, and Bader charge of this process are shown in Fig. 3c,e,f and
225 Supplementary Fig. 10. Since the (0001) facet is Li deficient, the O–O moiety is already closer to a
226 superoxide in terms of initial O–O bond length and Bader charge. According to these measures,
227 the central O–O moiety becomes superoxide-like and isolated $O_2$ after losing two Li and six Li,
228 respectively. Charge redistribution is again seen by the bond length of surrounding O–O moieties
229 remaining close to the initial value, Supplementary Fig. 11. An overpotential of 0.78 V is required
230 to make the energy profile downhill for the entire process to take place spontaneously (Fig. 3d).
231 This predicts a second threshold at 0.78 V (or 3.74 V vs $Li/Li^+$) where $RM^{ox}$ oxidizing $Li_2O_2$ is expected
232 to accelerate further.

233 To confirm this hypothesis and to identify the second threshold experimentally, TEMPO was
234 used as the RM in TEGDME where we could manipulate $E_{TEMPO/TEMPO^+}$ to above 3.7 V. Figure 4
235 shows the measured rate constant over the full voltage range. The first threshold is followed by a
236 gradual increase up to ~3.7 V, where another steep acceleration followed with kinetics doubling.
237 This increase is centred around 3.74 V or an overpotential of 0.78 V and hence matches perfectly
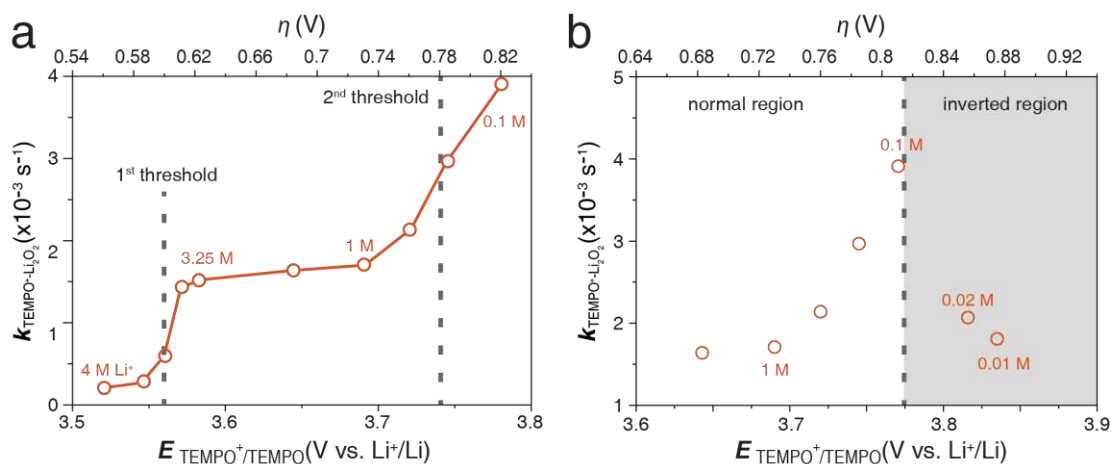238 the DFT prediction.

**Fig. 4 | Potential-dependent kinetics of TEMPO$^+$ oxidizing Li$_2$O$_2$ in tetraglyme over a wide range of $E_{\mathrm{TEMPO/TEMPO^+}}$. a,b,** TEMPO$^+$/TEMPO in tetraglyme electrolytes with various Li$^+$ concentrations from 0.1 M to 4 M (**a**) and 0.01 M to 0.1 M (**b**), where the kinetics decreases after passing a maximum. The dashed lines at 3.56 V and 3.74 V indicate the thresholds of TEMPO$^+$ oxidizing Li$_2$O$_2$.

Correctly predicting the two thresholds strongly supports the facet-dependent reaction pathways during mediated oxidation of Li$_2$O$_2$. To better understand the difference between these two facets, it is helpful to consider the reorganization energy $\Delta E^{j}_{\mathrm{reorg}}$ shown in Supplementary Fig. 10c. For (0001), the reorganization energy is $\approx$–0.4 V throughout, which arises from the symmetric structure of this facet. For (11$\overline{2}$0) in contrast, reorganization energies are $\approx$–0.9 V after the 4$^{th}$ and 5$^{th}$ step, where O–O bond length and Bader charger remain nearly constant. The weaker binding of the O–O moieties allows for large spatial reorganization and charge redistribution, which facilitates disproportionation.

Figure 4b not only shows the two thresholds rationalized by the facet-depending oxidation, but also decreasing kinetics beyond $\approx$3.77 V. Such behaviour is reminiscent of recently shown Marcus inverted region behaviour of peroxide oxidation with different RMs spanning a wide range of redox potentials[20]. Here, we see similar behaviour when the potential of a single RM was tuned using the Li$^+$ concentration. Marcus theory explains such decreasing kinetics despite increasing driving force by the overlap of discrete energy levels in the acceptor and donor[43,44]. A key descriptor herein is the total reorganization energy between initial and product states. Next to the reorganization energy of the Li$_2$O$_2$ slab as discussed above (Supplementary Fig. 10), it also accounts for the reorganization of the RM and the solvation shell of both reaction partners. Given the complicated multi-step delithiation process until eventual O$_2$ release, rigorous treatment following Marcus theory is beyond the scope of the work, but we suggest that the underlying ideas explain the decreasing kinetics observed here. Overall, the two thresholds and the observed maximum establish target potentials for maximum rates.

**Accelerated kinetics in operation**

To test the impact of the potential thresholds on batteries, we charged electrodes preloaded with commercial Li$_2$O$_2$ using 10 mM TBAI in DMSO containing 1 M or 0.05 M LiTFSI, where the

270  $I^-/I_3^-$ couple operates below/above the threshold potential. These Li$^+$ concentrations provide in

271  either case sufficient conductivity. If anything, the somewhat lower conductivity of the 0.05 M

272  (higher potential) electrolyte would lessen the effect of accelerated kinetics. Cells were charged

273  using linear sweep voltammetry and O$_2$ evolution followed by DEMS, Fig. 5. Cells without RM

274  served as base case for direct electrooxidization of Li$_2$O$_2$, Supplementary Fig. 12. Given that above

275  3.6 V I$_3^-$ is further oxidized to I$_2$, only the O$_2$ evolution below 3.6 V (indicated by the shaded region)

276  is taken to judge kinetics. I$^-$ in 1 M Li$^+$ electrolyte roughly doubled the O$_2$ yield compared to absence

277  of the mediator (Fig. 5b, Supplementary Fig. 12b). Lifting $E_{I^-/I_3^-}$ above the threshold with 0.05 M

278  Li$^+$ raised the O$_2$ yield by as much as 5-fold (Fig. 5a), confirming strongly boosted mediated kinetics

279  above the identified threshold.
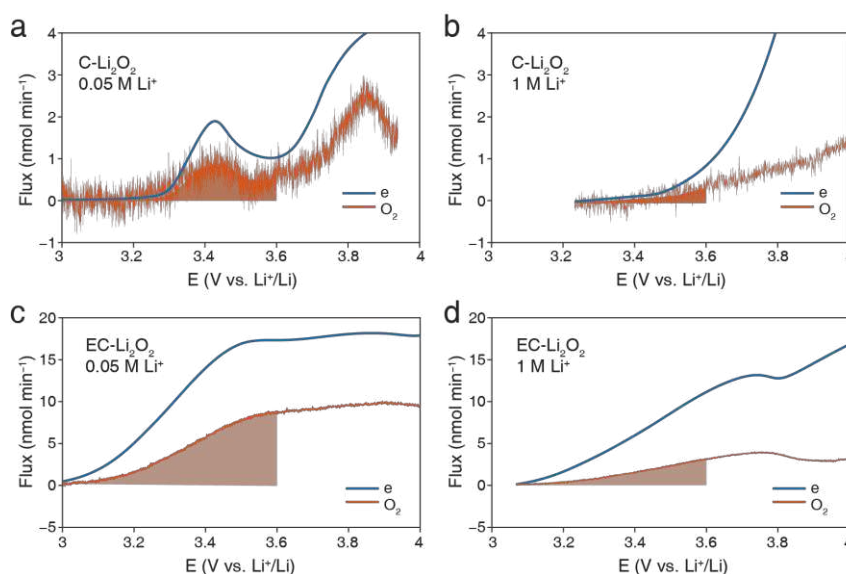


281  **Fig. 5 | *In-situ* DEMS during mediated charging. a**, **b**, Composite electrodes containing commercial Li$_2$O$_2$ (C–Li$_2$O$_2$)

282  and (c)(d) electrochemical-formed Li$_2$O$_2$ (EC–Li$_2$O$_2$) were charged in DMSO with 10 mM TBAI and the indicated Li$^+$

283  concentrations. 0.05 M and 1 M Li+ place $E_{I^-/I_3^-}$ above/below the threshold potential, respectively. The sweep

284  rate was 0.05 mV/s. The shaded regions represent the O$_2$ evolution by the I$_3^-$/I$^-$ redox couple below 3.6 V.

286  Electrochemically formed Li$_2$O$_2$ may expose dominant facets to different extend than

287  chemically formed (commercial) Li$_2$O$_2$. We therefore did the same experiments except for forming

288  the Li$_2$O$_2$ by discharging the electrodes in DMSO electrolyte, Fig. 5c,d and Supplementary Fig. 12c,d.

289  At low mediator potential (1 M Li$^+$), the O$_2$ yield doubled against the control without RM while it

290  was boosted more than 5-fold at a high mediator potential (0.05 M Li$^+$). Analogous results in cells

291  using chemically and electrochemically formed Li$_2$O$_2$ are all in accord with boosted kinetics beyond

292  the threshold that is related with the dominant $(11\overline{2}0)$ facet.

293  The effect is further confirmed using galvanostatic cycling of cells with the same I$^-$ containing

294  electrolytes, Supplementary Fig. 13. In line with above results, the charging overpotential with

295  lower Li$^+$ concentration (higher $E_{I^-/I_3^-}$) is lower than that with the high Li$^+$ concentration. The

296  charging plateau is with ~3.6 V only slightly above the threshold of 3.56 V. The higher oxidation

297  rate constant allows a smaller overpotential being sufficient to produce a RM$^{ox}$ concentration

298   capable of oxidizing $Li_2O_2$ at the applied current. This threshold or switch-on effect with $I^-$ only

299   takes $E_{I^-/I_3^-}$ to grow by 10 mV, which we have shown can arise from factors such as $Li^+$

300   concentration and type of solvents. Therefore, unintentionally positioning $E_{I^-/I_3^-}$ below or above

301   the threshold may explain some contradictory conclusions and debates about the capability of $I_3^-$

302   oxidizing $Li_2O_2$ during the charging process in literature[35,45], which span from highly active to nearly

303   inactive.

**Conclusions**

305        In summary, we have shown that the kinetics of mediators oxidizing insulating solids such as

306   $Li_2S$, and $Li_2O_2$ show distinct potential thresholds, where reaction kinetics accelerate several-fold.

307   The step in kinetics happens over a potential change of as little as 10 mV. For mediated $Li_2S$

308   oxidation, at threshold at 2.99 V (vs $Li^+$/Li) was found, where kinetics accelerated 4.4-fold. For $Li_2O_2$,

309   kinetics increased several-fold at thresholds at 3.56 V and 3.74 V. This phenomenon is independent

310   of the RM and the types of electrolyte. To clarify the origin, we determined the dominant crystal

311   facets of $Li_2O_2$ and examined with DFT the oxidation of the dominant $(11\bar{2}0)$ and (0001) facets.

312   Theoretical overpotentials to activate fast $Li^+/e^-$ extraction followed by $O_2$ release via

313   disproportionation are different at these facets and match the experimentally determined

314   threshold potentials. Disproportionation as the $O_2$ releasing step requires charge redistribution

315   between adjacent, increasingly Li-deficient O–O moieties at the peroxide surface. Facets where

316   these can move more easily such as the $(11\bar{2}0)$ experience larger stabilization by reorganization

317   and tend to be oxidized at lower overpotential.

318        For mediated oxidation to be fastest, the mediator should exceed the threshold potentials of

319   dominant facets. Adjusting the potential and boosting rate capability may be as simple as reducing

320   the $Li^+$ concertation as long as ionic conductivity remains sufficient. The results resolve

321   contradictory conclusions in the literature about the ability of the $I_3^-/I^-$ redox couple to oxidize $Li_2O_2$.

322   We give a rational for the most effective use of RMs to oxidize insulating active materials such as

323   those in metal-sulfur, metal-air, or metal-$CO_2$ batteries. The properties and abundance of individual

324   facets of the solid product determine required RM potentials for maximum charging rates.

325

**Methods**

327        **Materials and syntheses.** Chemicals were from Sigma Aldrich and used without further

328   purification. Lithium Superionic Conductor (LiSICON) was from Ohara. Gas diffusion layer (GDL)

329   electrodes (Freudenberg, H2315) were from Quintech. DMSO was distilled under vacuum and DME was

330   distilled under argon. All the solvents were further dried for several days with activated type 4Å

331   molecular sieves in an Ar-filled glove box. The molecular sieves (Aladdin) were first washed with ethanol,

332   dried in the furnace at 550 °C for 5 hours, and then placed in a drying tube and further dried at 300 °C

333   with a Büchi oven under vacuum for 24 h and   transferred into an Ar-filled glovebox without exposure

334   to air. The final water content of the DMSO and DME after drying was < 4 ppm (determined using a

335   Mettler Toledo Karl Fischer titrator). Bistrifluoromethanesulfonimide lithium (LiTFSI) was dried under

vacuum for 24 h at 120 °C. TEMPO$^+$ was prepared by electrolysis in a glass H-cell with a carbon paper working electrode, a commercial AgCl/Ag-acetonitrile reference electrode, and a graphite rod counter electrode. The working and counter electrode were separated with a sintered glass frit. 20 mM TEMPO in 0.1 M LiTFSI/tetraglyme served as anolyte at the working electrode and 0.1 M LiTFSI-tetraglyme served as catholyte at the counter electrode. Both electrolytes were stirrd. Firstly, the redox potential of TEMPO$^+$/TEMPO was determined by using cyclic voltammetry (CV) using an electrochemical workstation (VMP3, Biologic, France) with a planar glassy carbon disc electrode (diameter 3mm). Then the carbon paper working electrode was held at 400 mV positive to the redox potential of TEMPO to obtain TEMPO$^+$. Finally, the concentration of TEMPO$^+$ was determined using CV and found to be around 8 mM.

Amorphous $Li_2O_2$ was synthesized via a rapid disproportionation reaction of tetramethyl-ammonium superoxide ($TMAO_2$) and $LiClO_4$ in acetonitrile in an Ar-filled glove box as described previously[1]. $TMAO_2$ was prepared according to the solid reaction: $[(Me_4N)OH] \cdot H_2O + 3\ KO_2 \rightarrow (Me_4N)O_2 + 3/2\ O_2 + 3\ KOH$. Briefly, 10.9 g $[(Me_4N)OH] \cdot H_2O$ and 35 g $KO_2$ (5-fold excess $(Me_4N)OH \cdot H_2O$) were ground separately in mortars to fine powders in an Ar-filled glove box and then transferred to a 500 mL round-bottom flask with 20 g of 3 mm-diameter glass beads. The mixture was stirred with an overhead stirrer in the glovebox for a week. Finally, the mixture was transferred into a Soxhlet extractor and $TMAO_2$ was extracted using liquid ammonia. 2.3 g $TMAO_2$ was obtained and sealed under vacuum prior to transfer to the glovebox.

**Characterizations.** For the surface characterizations, the $Li_2O_2$ disk was immersed in DMSO for 10 minutes for TOF-SIMS experiments. Both a pristine disk and a treated disk were characterized with TOF-SIMS 5-100 (ION-TOF GmbH). X-ray diffraction (XRD) was carried out in an air-tight holder with a low-background Si substrate at a Bruker D4 X-ray diffractometer (Bruker, Germany) with Ni-filtered Cu K$_\alpha$ radiation (40 kV, 40 mA). The morphology of commercial $Li_2O_2$ was characterized by TEM (JEOL JEM 2100).

The kinetics of DFc$^+$ oxidizing $Li_2S$ is measured by using UV-vis spectroscopy. The DFc$^+$ solution was prepared by electrolysis of 10 mM DFc in 0.1 M LiTFSI/DME in a homemade H-type cell with a piece of LiSICON solid state electrolyte to separate the catholyte and anolyte and a carbon paper working electrode and a Li counter electrode. The final concentration of DFc$^+$ was determined using CV. 3mL of solution containing a known concentration of DFc$^+$ was injected to an air–tight cuvette containing 10 mg of $Li_2S$ under stirring in an Ar-filled glovebox. After reaction with several minutes, the suspension is centrifuged briefly and the UV-vis spectra of the clear solution was recorded. The remaining concentrations of DFc$^+$ after reaction were determined form the absorption peak at 780 nm and $-\ln A_{780nm}$ was plotted versus the reaction time, Supplementary Fig. 2. The rate constant ($k_{\mathrm{DFc-Li_2S}}^{\mathrm{app}}$) was obtained from the slope of the data fit as 1$^{st}$ order reaction. The polysulfide solution was prepared by stirring the $S_8$ powder and $Li_2S$ together in DME overnight. $Li_2S$ reacted with $S_8$ to form polysulfides.

372 The suspension was centrifuged and then the brownish supernatant was collected. The DFc$^+$ solution

373 was injected into the polysulfide solution and then colour of DFc$^+$ faded out rapidly within 150 s,

374 Supplementary Fig. 3.

375 **Electrochemical methods.** The differential electrochemical mass spectrometry (DEMS) system was

376 based on a commercial magnet-sector mass spectrometer (Thermo Fischer, Prima BT) and guided by

377 the requirement to quantify all the gases evolved during the charging process. The DEMS cell was based

378 on a customized Swagelok-type cell providing air-tightness, as discussed previously[2]. In the DEMS

379 experiments of I$_3^-$ oxidizing Li$_2$O$_2$, 0.8 ml of various solutions containing 4 mM TBAI$_3$ were injected into

380 a vial containing an excess amount of Li$_2$O$_2$. The evolved O$_2$ was quantified using DEMS. Pure Ar was

381 used as a carrier gas and the flow rate was typically 1 mL/min. Kinetics measurements are discussed in

382 Supplementary Note 1. Typically, 9 mg of Li$_2$O$_2$ was used. In the experiment of TBAI$_3$ oxidizing LiOH,

383 Li$_2$CO$_3$, Li formate, and Li acetate, the same experiments were carried out with Li$_2$O$_2$ being replaced by

384 these compounds. In the experiments of TEMPO$^+$ oxidizing Li$_2$O$_2$, 0.8 ml of 8 mM TEMPO$^+$ in tetraglyme

385 with various Li$^+$ concentrations between 3.25 M and 4 M Li$^+$ were injected into a vial containing 9 mg

386 Li$_2$O$_2$ and the O$_2$ evolution was quantified.

387 *In-situ* DEMS experiments were carried out with electrodes preloaded with commercial Li$_2$O$_2$ or

388 electrochemically formed Li$_2$O$_2$ (EC-Li$_2$O$_2$). To load commercial Li$_2$O$_2$, 10 mg Li$_2$O$_2$ were dispersed in 5 ml

389 of DME by stirring and ultra-sonication. Then 50 µl of the suspension were dropped onto a GDL

390 electrode (12 mm diam.). The wet electrode is dried under vacuum and the same procedure repeated

391 several times. The mass loading of Li$_2$O$_2$ was 1 mg cm$^{-2}$. To load EC-Li$_2$O$_2$, the electrode was discharged

392 in 1 M LiTFSI tetraglyme electrolyte saturated with O$_2$ to a capacity of 1.16 mAh cm$^{-2}$ (corresponding to

393 1 mg$_{Li2O2}$ cm$^{-2}$). The electrodes with Li$_2$O$_2$ were charegd using a linear voltage sweep from OCV to 4 V

394 (vs. Li$^+$/Li) at a sweep rate of 0.05 mV/s. Pure Ar worked as carrier gas at a flow rate of 0.3 ml/min.

395 Scanning Electrochemical Microscope (SECM) approach curves towards a Li$_2$O$_2$ pellet were

396 measured with a CHI 900D SECM in an Ar-filled glovebox as described previously[3]. Li$_2$O$_2$ disks were

397 obtained by pressing Li$_2$O$_2$ powder with a die set press in an Ar-filled glove box. Disks of 13 mm diameter

398 and ~1 mm thickness were prepared and served as substrate. An Au microelectrode (diam. 25 µm, CHI)

399 served as the SECM probe. Prior to the measurements, the Au tip was polished with a homemade

400 microelectrode beveller and checked with a microscope. A silver wire reference electrode (RE) and a

401 platinum counter electrode (CE) were used. The data processing and fitting process were described

402 elsewhere[4]. A dimensionless rate constant, κ, was obtained by data fit, which equals to $\frac{k^{app}\ r_0}{D}$, where

403 $r_0$ is the radius of tip, $D$ is the diffusion coefficient of redox mediator, and $k^{app}$ the apparent

404 heterogeneous rate constant.

405 $E_{\mathrm{DFc/DFc^+}}$ and $E_{\mathrm{TEMPO/TEMPO^+}}$ (vs Li$^+$/Li) in various electrolytes were measured by CV using a

406 three-electrode configuration using a glassy carbon working electrode and a graphite rod counter

407 electrode. The piece of partially delithiated Li$_{1-x}$FePO$_4$ composite electrode inside a glass tube with a frit

408  at the end was used as the reference electrode, which provided a constant potential of 3.45 V vs Li⁺/Li.

409  The reference electrode was filled with the same electrolyte as the working electrode but without a

410  redox mediator. Because the $I_3^-/I^-$ redox couple does not show a pair of symmetric redox peaks, $E_{I^-/I_3^-}$

411  in various solvents was calculated from the open-circuit voltage (OCV). A solution containing 10 mM

412  TBAI₃ and 10 mM TBAI was prepared with various concentrations of LiTFSI. The OCV was recorded and

413  the $E_{I^-/I_3^-}$ (vs Li⁺/Li) can be calculated from $E_{OCV}$ by the Nernst equation:

414
$$E_{OCV} = E_{I_3^-/I^-} + \frac{RT}{2F} \ln \frac{c_{TBAI_3}}{(c_{TBAI})^3} \tag{S1}$$

415

416  Cycling performance was measured with homemade Swagelok-type cells assembled in an Ar-filled glove

417  box. Super P-PTFE (9:1, wt%) was sprayed with a mass loading of 0.5 mg/cm² on GDL as cathode. The

418  anode was Li metal. The electrodes were separated by a LiSICON glass to prevent the shuttling and

419  short-circuit of RMs. The iR drop caused by LiSICON was corrected in the load curves. 10 mM TBAI-

420  DMSO with 0.05 M or 1 M LiTFSI was used as catholyte and 0.5 M LiTFSI-DME as anolyte. The cells were

421  cycled at a current density of 0.2 mA/cm² in 1 atm of O₂.

422  **Density Functional Theory (DFT) calculations.** DFT calculations were conducted within the Vienna Ab-

423  initio Simulation Package (VASP)[5,6] The potentials were of the projector plane wave (PAW) type,[7] and

424  the exchange-correlation part of the density functional was treated within the generalized gradient

425  approximation (GGA) of Perdew–Burke–Ernzerhof (PBE).[8] We used plane-wave cutoff energy of 500

426  eV and 1×1×1 Monkhorst–Pack k-point mesh[9] with Gaussian smearing of 0.05 eV [10] to relax the

427  electronic energies and nuclear degrees of freedom. The electronic structure was optimized within an

428  error of $10^{-6}$ eV/atom and the geometry was optimized to force tolerance of 0.03 eV/Å. The spin-

429  polarization was considered and DFT-D3 method[11] with Becke-Jonson damping[12] was applied to

430  describe the van der Walls (vdW) interactions. Procedures of all the calculations were implemented in

431  the computational platform for battery materials.[13]

432  For examining the decomposition mechanisms of Li₂O₂ on the $(11\bar{2}0)$ facet, a slab supercell (2×2)

433  with 5 layers containing 160 atoms was constructed from a hexagonal unit cell (a = 3.12 Å, c = 7.56 Å)

434  and the vacuum slab was set to 20 Å to eliminate the ramped electron interaction between slabs due

435  to the periodic system. Two layers were fixed to mimic the bulk structure. The path starts with Li⁺

436  removal from the surface structure and ends with O₂ evolution, covering both the electrochemical (the

437  desorption of Li⁺) and the chemical (the desorption of O₂) steps. As long as the process is energy

438  favorable, the O-O dimer could be removed at any stage and the energy required is shown in

439  Supplementary Fig. 10. The details will be discussed below.

440  First, we calculated the redox potential of the bulk Li₂O₂ decomposition according to the reaction
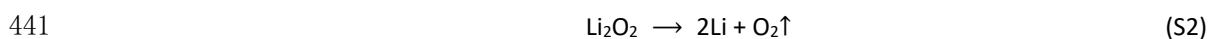
441
$$\text{Li}_2\text{O}_2 \longrightarrow 2\text{Li} + \text{O}_2\uparrow \tag{S2}$$
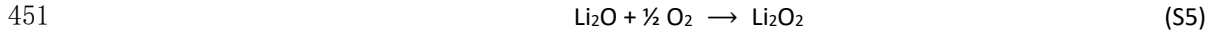
The reaction free energy of the above reaction is

$$\Delta G = G(\text{Li}) + G(\text{O}_2) - G(\text{Li}_2\text{O}_2) \tag{S3}$$

where the Gibbs free energies of Li and $\text{Li}_2\text{O}_2$ are calculated according to

$$G = E + ZPE + \Delta H_{\text{expt}}^{0 \to 298.15K} - TS_{\text{expt}}^{0 \to 298.15K} \tag{S4}$$

where the $E$ is the electronic energy obtained from the DFT calculations, ZPE is the zero-point energy, $\Delta H_{\text{expt}}^{0 \to 298.15K}$ and $S_{\text{expt}}^{0 \to 298.15K}$ are the experimental enthalpy and entropy variation from 0 K to 298.15 K, respectively.[14] $T$ is 298.15 K.

$\text{O}_2$ (1 atm, 298.15 K) was corrected by the following reaction due to the overestimate of the binding energy by DFT:

$$\text{Li}_2\text{O} + \tfrac{1}{2}\,\text{O}_2 \longrightarrow \text{Li}_2\text{O}_2 \tag{S5}$$

Based on the experimental reaction energy of the above reaction ($\Delta G_r^{\text{expt}}$) and the calculated Gibbs free energies of $\text{Li}_2\text{O}$ and $\text{Li}_2\text{O}_2$, which are involved in the correction of the zero-point energy and the experimental enthalpy and entropy,[46] we determine the chemical potential of oxygen according to

$$\mu(\text{O}) = G(\text{Li}_2\text{O}_2) - G(\text{Li}_2\text{O}) - \Delta G_r^{\text{expt}} \tag{S6}$$

Thus, the Gibbs free energy of $\text{O}_2$ is

$$G(\text{O}_2) = 2\ \mu(\text{O}) + ZPE + \Delta H_{\text{expt}}^{0 \to 298.15K} - TS_{\text{expt}}^{0 \to 298.15K} \tag{S7}$$

where the enthalpy and entropy are referred to as the thermochemical dataset.[46] $T$ is 298.15K. Then the theoretical redox potential ($U$) can be calculated by:

$$U = -\Delta G / nF \tag{S8}$$

Following the above equations (S2)-(S8), we give the theoretical redox potential of 2.75 V for the bulk $\text{Li}_2\text{O}_2$ decomposition, close to the reported value in the literature (2.82 V)[15].

After obtaining the bulk redox potential, the next step is to explore the intrinsic barrier of the surface decomposition. It is widely accepted that the $\text{Li}_2\text{O}_2$ decomposition includes both the electrochemical step (the desorption of $\text{Li}^+$) and the chemical step (the desorption of $\text{O}_2$), respectively. The reaction energy of the $j^{th}$ ($j$ ranges from 1 to 7) electrochemical step ($\Delta E_e^j$) is defined as

$$\Delta E_e^j = E^j + E(\text{Li}) - E^{j-1} - eU \tag{S9}$$

where $E^j$ and $E^{j-1}$ are the energies of the $\text{Li}_2\text{O}_2$ slab after and before the desorption of Li, respectively, $E(\text{Li})$ is the energy of bulk Li, and $U$ is the predicted theoretical electrochemical potential. The chemical step for the $j^{th}$ step is defined as:

$$\Delta E_c^j = E_C^{j(j+2)} + E(\text{O}_2) - E_C^{j(j+1)} \tag{S10}$$

where $E_C^{j(j+2)}$ and $E_C^{j(j+1)}$ are the energies of the $\text{Li}_2\text{O}_2$ slab after and before the desorption of $\text{O}_2$, respectively. To cancel systematic errors, the reference $E(\text{O}_2)$ is the energy of the directly calculated energy of $\text{O}_2$ in the gas phase without correction. Note that the $\text{O}_2$ which is about to desorb is in an

isolated state and physically adsorbed at the surface as confirmed by the differential charge density (Supplementary Fig. 10). It can be seen that there is almost no charge density between the $O_2$ and the matrix, suggesting that the $O_2$ in the surface described by DFT is similar to the directly calculated state in DFT within a supercell, which we chose a sufficiently large cubic cell (20×20×20 Å$^3$) to mimic the process taking place at an extended surface.

Correspondingly, the overpotential ($\eta$) is defined as

$$\eta = \max\{\Delta E_e^j / e\} \qquad\qquad (S11)$$

It is worth mentioning that the conventional reaction profiles are confined to a single or two $Li_2O_2$ formula(s)[15-17], thus including only three steps (Li↑-$O_2$↑-Li↑ or Li↑-Li↑-$O_2$↑, where the up-arrow denotes the desorption) or a repeat of these three steps to maintain the ratio of desorbed Li atoms to $O_2$ molecules at 2:1. In such a path, the reaction energy of the chemical step is up to 1.8 eV,[39] which is impossible to overcome by the energy oscillation, implying a non-spontaneous process. In other words, the conventional reaction profiles are non-spontaneous.

Herein, based on the consideration that the exploration of the path should not be limited to the stoichiometric formulas, $i.e.$, the ratio of desorbed Li atoms to $O_2$ molecules can exceed 2:1, we demonstrate that the rate-determining step (rds) is the electrochemical desorption of Li rather than the chemical desorption of $O_2$. Figure 3 shows an irregular but more feasible path followed during the decomposition process at the conversion reaction cathode, where the decomposition occurs from the electrochemical step until the surface becomes amorphous and the chemical step is no longer the rds. Figure 3f shows the dependence of the chemical reaction energy ($\Delta E_c^j$) for the desorption of $O_2$ after removal of $j$ Li. It is seen that $\Delta E_c^j$ drops from 1.82 to 0.20 eV as the number of the electrochemical Li extractions increased from 2 to 7. This barrier of 0.2 eV is sufficiently small to be easily overcome by thermal oscillations. Also, compared with the electrochemical step (0.63 eV), the chemical step (0.20 eV) is no longer the rds. These results in turn demonstrate that the required driving force during charging is dictated by the electrochemical potential barrier.

**References**

1    Choi, J. W. & Aurbach, D. Promise and reality of post-lithium-ion batteries with high energy densities. *Nat. Rev. Mater.* **1**, 16013, doi:10.1038/natrevmats.2016.13 (2016).

2    Qiao, Y., Jiang, K., Deng, H. & Zhou, H. A high-energy-density and long-life lithium-ion battery via reversible oxide–peroxide conversion. *Nature Catalysis* **2**, 1035-1044, doi:10.1038/s41929-019-0362-z (2019).

3    Cameron, J. M. *et al.* Molecular redox species for next-generation batteries. *Chem. Soc. Rev.*, doi:10.1039/D0CS01507E (2021).

4    Kwak, W.-J. *et al.* Lithium–Oxygen Batteries and Related Systems: Potential, Status, and Future. *Chem. Rev.*, doi:10.1021/acs.chemrev.9b00609 (2020).

511   5    Ko, Y. *et al.* Anchored Mediator Enabling Shuttle-Free Redox Mediation in Lithium-Oxygen
512        Batteries. *Angew. Chem. Int. Ed.* **59**, 5376-5380, doi:10.1002/anie.201916682 (2020).
513   6    Wang, Y. & Lu, Y.-C. Nonaqueous Lithium–Oxygen batteries: Reaction mechanism and critical
514        open questions. *Energy Storage Materials* **28**, 235-246, doi:10.1016/j.ensm.2020.03.007 (2020).
515   7    Wu, S. *et al.* Organic hydrogen peroxide-driven low charge potentials for high-performance
516        lithium-oxygen batteries with carbon cathodes. *Nat. Commun.* **8**, 15607,
517        doi:10.1038/ncomms15607 (2017).
518   8    Qiao, Y. *et al.* Li-CO$_2$ Electrochemistry: A New Strategy for CO$_2$ Fixation and Energy Storage.
519        *Joule*, doi:10.1016/j.joule.2017.07.001 (2017).
520   9    Lu, Y.-C., He, Q. & Gasteiger, H. A. Probing the Lithium–Sulfur Redox Reactions: A Rotating-
521        Ring Disk Electrode Study. *J. Phys. Chem. C* **118**, 5733-5741, doi:10.1021/jp500382s (2014).
522  10    Bonnick, P. & Muldoon, J. The Dr Jekyll and Mr Hyde of lithium sulfur batteries. *Energy Environ.*
523        *Sci.* **13**, 4808-4833, doi:10.1039/D0EE02797A (2020).
524  11    Kwak, W.-J. *et al.* Controllable and stable organometallic redox mediators for lithium oxygen
525        batteries. *Materials Horizons* **7**, 214-222, doi:10.1039/C9MH01043B (2020).
526  12    Park, J.-B., Lee, S. H., Jung, H.-G., Aurbach, D. & Sun, Y.-K. Redox Mediators for Li–O$_2$ Batteries:
527        Status and Perspectives. *Adv. Mat.* **30**, 1704162, doi:10.1002/adma.201704162 (2018).
528  13    Kwak, W.-J., Kim, H., Jung, H.-G., Aurbach, D. & Sun, Y.-K. Review—A Comparative Evaluation
529        of Redox Mediators for Li-O$_2$ Batteries: A Critical Review. *J. Electrochem. Soc.* **165**, A2274-
530        A2293, doi:10.1149/2.0901810jes (2018).
531  14    Meini, S., Elazari, R., Rosenman, A., Garsuch, A. & Aurbach, D. The Use of Redox Mediators for
532        Enhancing Utilization of Li$_2$S Cathodes for Advanced Li–S Battery Systems. *J. Phys. Chem. Lett.*
533        **5**, 915-918, doi:10.1021/jz500222f (2014).
534  15    Pande, V. & Viswanathan, V. Criteria and Considerations for the Selection of Redox Mediators
535        in Nonaqueous Li–O$_2$ Batteries. *ACS Energy Lett.* **2**, 60-63, doi:10.1021/acsenergylett.6b00619
536        (2017).
537  16    McCloskey, B. D. *et al.* Twin Problems of Interfacial Carbonate Formation in Nonaqueous Li–O$_2$
538        Batteries. *J. Phys. Chem. Lett.* **3**, 997-1001, doi:10.1021/jz300243r (2012).
539  17    Wang, Y., Lu, Y.-R., Dong, C.-L. & Lu, Y.-C. Critical Factors Controlling Superoxide Reactions in
540        Lithium–Oxygen Batteries. *ACS Energy Lett.*, 1355-1363, doi:10.1021/acsenergylett.0c00365
541        (2020).
542  18    Liang, Z., Zhou, Y. & Lu, Y.-C. Dynamic oxygen shield eliminates cathode degradation in lithium–
543        oxygen batteries. *Energy Environ. Sci.* **11**, 3500-3510, doi:10.1039/C8EE02067A (2018).
544  19    Gao, X., Chen, Y., Johnson, L. R., Jovanov, Z. P. & Bruce, P. G. A rechargeable lithium–oxygen
545        battery with dual mediators stabilizing the carbon cathode. *Nat. Energy* **2**, 17118,
546        doi:10.1038/nenergy.2017.118 (2017).
547  20    Petit, Y. K. *et al.* Mechanism of mediated alkali peroxide oxidation and triplet versus singlet
548        oxygen formation. *Nat. Chem.* **13**, 465–471, doi:10.1038/s41557-021-00643-z (2021).
549  21    Liang, Z. & Lu, Y.-C. Critical Role of Redox Mediator in Suppressing Charging Instabilities of
550        Lithium–Oxygen Batteries. *J. Am. Chem. Soc.* **138**, 7574-7583, doi:10.1021/jacs.6b01821
551        (2016).
552  22    Kwak, W.-J. *et al.* Deactivation of redox mediators in lithium-oxygen batteries by singlet oxygen.
553        *Nat. Commun.* **10**, 1380, doi:10.1038/s41467-019-09399-0 (2019).
554  23    Liang, Z., Zou, Q., Xie, J. & Lu, Y.-C. Suppressing singlet oxygen generation in lithium–oxygen

batteries with redox mediators. *Energy Environ. Sci.* **13**, 2870-2877, doi:10.1039/D0EE01114B (2020).

24    Mu, X., Pan, H., He, P. & Zhou, H. Li–CO₂ and Na–CO₂ Batteries: Toward Greener and Sustainable Electrical Energy Storage. *Adv. Mat.* **32**, 1903790, doi:https://doi.org/10.1002/adma.201903790 (2020).

25    Zhao, M., Chen, X., Li, X. Y., Li, B. Q. & Huang, J. Q. An Organodiselenide Comediator to Facilitate Sulfur Redox Kinetics in Lithium-Sulfur Batteries. *Adv. Mat.* **33**, doi:10.1002/adma.202007298 (2021).

26    Zhao, M. *et al.* Redox Comediation with Organopolysulfides in Working Lithium-Sulfur Batteries. *Chem* **6**, 3297-3311, doi:10.1016/j.chempr.2020.09.015 (2020).

27    Tsao, Y. *et al.* Designing a Quinone-Based Redox Mediator to Facilitate Li₂S Oxidation in Li-S Batteries. *Joule*, doi:10.1016/j.joule.2018.12.018.

28    Chen, Y., Gao, X., Johnson, L. R. & Bruce, P. G. Kinetics of lithium peroxide oxidation by redox mediators and consequences for the lithium–oxygen cell. *Nat. Commun.* **9**, 767, doi:10.1038/s41467-018-03204-0 (2018).

29    Henstridge, M. C., Laborda, E., Rees, N. V. & Compton, R. G. Marcus–Hush–Chidsey theory of electron transfer applied to voltammetry: A review. *Electrochim. Acta* **84**, 12-20, doi:10.1016/j.electacta.2011.10.026 (2012).

30    Wild, M. *et al.* Lithium sulfur batteries, a mechanistic review. *Energy Environ. Sci.* **8**, 3477-3494, doi:10.1039/C5EE01388G (2015).

31    Wang, Y. *et al.* A Solvent-Controlled Oxidation Mechanism of Li₂O₂ in Lithium–Oxygen Batteries. *Joule* **2**, 2364-2380, doi:10.1016/j.joule.2018.07.021 (2018).

32    Zou, Q. & Lu, Y.-C. Solvent-Dictated Lithium Sulfur Redox Reactions: An Operando UV–vis Spectroscopic Study. *J. Phys. Chem. Lett.* **7**, 1518-1525, doi:10.1021/acs.jpclett.6b00228 (2016).

33    Ko, Y. *et al.* A comparative kinetic study of redox mediators for high-power lithium–oxygen batteries. *J. Mat. Chem. A* **7**, 6491-6498, doi:10.1039/C9TA00096H (2019).

34    Bawol, P. P. *et al.* A new thin layer cell for battery related DEMS-experiments: the activity of redox mediators in the Li–O₂ cell. *Phys. Chem. Chem. Phys.* **20**, 21447-21456, doi:10.1039/C8CP03592J (2018).

35    Leverick, G., Tułodziecki, M., Tatara, R., Bardé, F. & Shao-Horn, Y. Solvent-Dependent Oxidizing Power of LiI Redox Couples for Li–O₂ Batteries. *Joule* **3**, 1106-1126, doi:10.1016/j.joule.2018.12.014 (2019).

36    Zhang, Y. *et al.* Amorphous Li₂O₂: Chemical Synthesis and Electrochemical Properties. *Angew. Chem. Int. Ed.* **55**, 10717-10721, doi:10.1002/anie.201605228 (2016).

37    Kang, S., Mo, Y., Ong, S. P. & Ceder, G. A Facile Mechanism for Recharging Li₂O₂ in Li–O₂ Batteries. *Chem. Mat.* **25**, 3328–3336, doi:10.1021/cm401720n (2013).

38    Hummelshoj, J. S., Luntz, A. C. & Norskov, J. K. Theoretical evidence for low kinetic overpotentials in Li-O₂ electrochemistry. *J. Chem. Phys.* **138**, 034703 (2013).

39    Zhu, J., Ren, X., Liu, J., Zhang, W. & Wen, Z. Unraveling the Catalytic Mechanism of Co3O4 for the Oxygen Evolution Reaction in a Li–O2 Battery. *ACS Catal.* **5**, 73-81, doi:10.1021/cs5014442 (2015).

40    Zhu, J. *et al.* Surface Acidity as Descriptor of Catalytic Activity for Oxygen Evolution Reaction in Li-O2 Battery. *J. Am. Chem. Soc.* **137**, 13572-13579, doi:10.1021/jacs.5b07792 (2015).

41    Mourad, E. *et al.* Singlet oxygen from cation driven superoxide disproportionation and

599  consequences for aprotic metal–O$_2$ batteries. *Energy Environ. Sci.* **12**, 2559-2568,
600  doi:10.1039/C9EE01453E (2019).
601  42  Mahne, N. *et al.* Singlet oxygen generation as a major cause for parasitic reactions during cycling
602  of aprotic lithium–oxygen batteries. *Nat. Energy* **2**, 17036, doi:10.1038/nenergy.2017.36 (2017).
603  43  Marcus, R. A. Electron transfer reactions in chemistry. Theory and experiment. *Rev. Mod. Phys.*
604  **65**, 599-610, doi:10.1103/RevModPhys.65.599 (1993).
605  44  Savéant, J.-M. & Constentin, C. *Elements of molecular and biomolecular electrochemistry*. 2$^{nd}$
606  edn,   (John Wiley & Sons, 2019).
607  45  Burke, C. M. *et al.* Implications of 4 e$^-$ Oxygen Reduction via Iodide Redox Mediation in Li–O$_2$
608  Batteries. *ACS Energy Lett.* **1**, 747-756 (2016).
609  46  Chase, M. W.   (American Institute of Physics: Melville, NY, 1998).
610

**Acknowledgments**

**Author contributions**

Y.C., S.S. and S.A.F. conceived and directed the project. D.C., X.S., A.W. and F.Y. performed experiments and DFT calculations. S.A.F, Y.C., and S.S wrote the manuscript. All authors discussed and revised the manuscript.

**Competing interests**

The authors declare no competing interests.

# Supplementary Files

This is a list of supplementary files associated with this preprint. Click to download.

- SupplementaryInformation.pdf